ORIGINAL RESEARCH ARTICLE

Effect of Phase-Selective Nanoscale Precipitates on the Bauschinger Effect in Austenitic–Ferritic Duplex Stainless Steels

M. KREINS, J. WILKES, S. WESSELMECKING, and U. KRUPP

The Bauschinger effect in austenitic–ferritic duplex stainless steel 1.4462 was investigated using tension–compression tests combined with electron backscatter diffraction (EBSD). A major focus was on the impact of phase-selective nanoscale α′ precipitates formed in the ferritic phase due to 475 °C embrittlement. Contrary to the general knowledge that coherent precipitates have only a short-range effect and thus no significant influence, a strong increase in the Bauschinger effect was detected. Based on EBSD data and cyclic micro-indentations in individual grains, it was demonstrated that α′ precipitates enhance the phase difference between austenite and ferrite and increase deformation incompatibility and local dislocation density gradients at phase boundaries. Thus, despite their small size and coherence, α′ precipitates lead to long-range back stresses that significantly enhance the Bauschinger effect. In addition, the influence of precipitation was shown to depend on the extent of pre-strain during initial loading. The insights demonstrate that the influence of precipitates on the Bauschinger effect is highly complex and always needs to be analyzed with respect to precipitation characteristics, microstructure, and external boundary conditions.

https://doi.org/10.1007/s11661-022-06793-0

I. INTRODUCTION

THE plasticity behavior of metallic materials during complex loading conditions is of high interest in numerous manufacturing processes and applications, *e.g.*, multi-stage forming processes and cyclic loading of mechanical components. In this context, the so-called Bauschinger effect is of importance, which describes a softening of metallic materials during load reversal.[1–3] The phenomenon is caused by the elastic–plastic anisotropy of multi-crystal arrangement and the resulting back stresses, which support deformation during load reversal.[4,5] In addition, a directional dependence of the mean free path length of dislocations as well as the dissolution of dislocation pile-ups in front of obstacles are considered.[6,7] The Bauschinger effect is influenced by numerous factors. In addition to exogenous factors such as temperature,[8] strain rate,[9] and amount of pre-strain,[10] the microstructure of the material is of particular importance.[11] Crystal structure and orientation, phase properties, and grain or phase boundaries influence the Bauschinger effect.[6,12–14] The effect of precipitates is particularly complex and has already been extensively studied on various alloys. Their impact depends on size, coherence, and number density.[15–17] Generally, two different categories are distinguished with respect to the type of dislocation interaction. Large incoherent precipitates, which are bypassed according to the Orowan mechanism, have a long-range effect and thus a large impact on Bauschinger effect.[18] Dislocation pile-up in front of precipitates generates back stresses, and the dissolution of Orowan rings during load reversal can also promote re-plasticization.[18,19] In contrast, small, coherent precipitates cut during initial loading have only a short-range effect. The recovery of antiphase boundaries (APBs) during load reversal can amplify the Bauschinger effect, but the impact is considered to be rather small.[18,20] The effect of small, coherent precipitates is therefore considered negligible in the literature.[17] But it is worth mentioning that previous studies have so far only analyzed the effect of homogeneously distributed precipitates. The effects of an inhomogeneous precipitation density have not yet been considered. However, local inhomogeneities and resulting back stresses could be of high importance for the Bauschinger effect. It is therefore hypothesized that even small, coherent precipitates with a short-range effect can significantly affect the Bauschinger effect if they are inhomogeneously distributed. Local gradients

M. KREINS, J. WILKES, S. WESSELMECKING, and U. KRUPP are with the IEHK Steel Institute, RWTH Aachen University, Intzestraße 1, 52072 Aachen, Germany. Contact e-mail: marion.kreins@iehk.rwth-aachen.de
Manuscript submitted April 27, 2022; accepted August 4, 2022.
Article published online September 7, 2022

in precipitation density might induce long-range back stresses, and thus enhance the macroscopic Bauschinger effect.

The effect of inhomogeneously distributed nanoscale coherent precipitates on the Bauschinger effect was investigated using the industrially widely used duplex stainless steel (DSS) 1.4462.[21–23] The two-phase microstructure is prone to various precipitation reactions, of which the well-known 475 °C embrittlement was applied.[21,24,25] Annealing at 475 °C for several hours leads to spinodal segregation of the ferrite into an iron-rich matrix and homogenously distributed chromium-rich α' precipitates, whereas the austenitic phase is not affected (Figure 1).[26,27] It is therefore possible to adjust a phase-selective and thus locally inhomogeneous precipitation distribution, which can be specifically modified by the choice of aging time. When analyzing the Bauschinger effect, however, it must be considered that DSS already shows very complex plasticity behavior and a pronounced Bauschinger effect in the precipitation-free as-rolled condition. Main reasons are the deformation incompatibility of ferrite and austenite as well as the partitioning of stress and strain, which has been extensively analyzed using various experimental methods like nano-hardness test and X-ray diffraction,[28] atomic force microscopy,[29] *in-situ* neutron diffraction,[30,31] electron backscatter diffraction analysis,[32,33] and simulative approaches.[34] However, load reversal and thus the Bauschinger effect are usually not considered. Studies of cyclic plasticity behavior of DSS, on the other hand, analyze high numbers of cycles and mainly address crack initiation and material damage.[35,35–37] Precise investigations of the Bauschinger effect in two-phase microstructures are rare and focus on individual aspects like the effect of chemical composition or phase ratio.[38,39]

Against this background, the following study can be divided into two major sections. First, the Bauschinger effect in the precipitation-free as-rolled condition of DSS 1.4462 is quantified and analyzed using tension–compression tests and electron backscatter diffraction (EBSD). The data contribute to the understanding of Bauschinger effect in multi-phase alloys and provides the reference state for the investigation of precipitation effects in the second part. Therein, the effect of phase-selective precipitates in ferrite will be analyzed by dislocation density distribution maps and micro-indentation tests in individual austenitic and ferritic grains. In addition, it is investigated whether the influence of the precipitates is affected by the level of the pre-strain during initial loading. The paper concludes with a quantification and explanation of the influence phase-selective precipitates and pre-strain on the Bauschinger effect in DSS 1.4462.

II. EXPERIMENTAL

Duplex stainless steel 1.4462 (provided as ''Acidur'' by Deutsche Edelstahlwerke Specialty Steel GmbH & Co. KG, corresponds to SAE2205) with the chemical composition given in Table I was investigated by tension–compression tests and EBSD measurements. The reference material was provided in solution-annealed and quenched condition according to standard DIN EN 10088-3[41] as round bars. In order to adjust phase-selective, nanoscale precipitates in the ferrite, samples were exposed to the well-known 475 °C embrittlement.[25,42] Therefore, heat treatments at 475 °C for 5 and 15 hours were conducted in a salt bath furnace using salt AS140 with an inhibitor to avoid surface depletion of carbon.

Mechanical properties after different heat treatments were checked by Vickers hardness test (HV10) according to standard DIN EN ISO 6507.[43] Round tension–compression test samples were manufactured parallel to rolling direction by milling with subsequent surface finishing by grinding. Due to the lack of standardization of tension–compression tests and the large number of different approaches in literature,[10,30,44,45] no generally

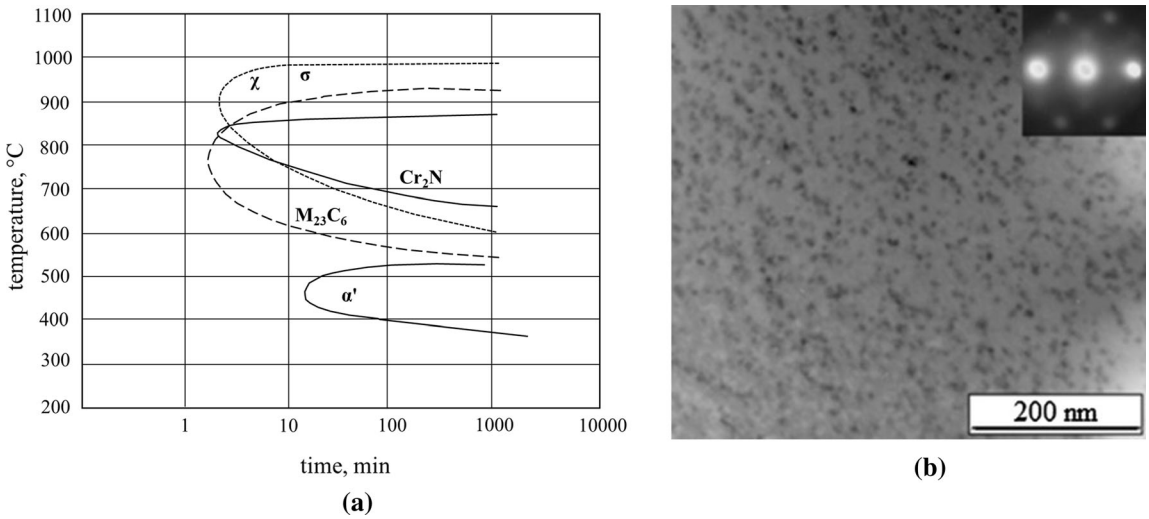

Fig. 1—(*a*) schematic TTT diagram of DSS 1.4462 (author's illustration according to supplier information); (*b*) TEM image of the ferrite in DSS 1.4462 after 475 °C embrittlement for 100 h, α' is visible as black areas. Reprinted with kind permission from Elsevier from Ref. [40].

accepted specimen geometry is established. In order to achieve the best possible comparability, round tensile specimens according to standard DIN 50125[46] for tensile tests were slightly modified to address the special requirements of tension–compression test. As shown in Figure 2, the parallel length was reduced to prevent buckling and the threads were lengthened to ensure fixed clamping in the testing machine.

The mechanical properties were evaluated by tensile tests and tension–compression tests at room temperature and a strain rate of 0.003 s^{-1} using a servo-hydraulic testing machine (Rumul Gigaforte 50). For each material condition and test parameter, at least 4 samples were tested for statistical validation. Strain measurement was carried out with a clip-on extensometer (Instron). The initial gauge length was 10 mm and length change was recorded with a measuring frequency of 5 Hz. Furthermore, local strain was detected by digital image correlation using a 3D camera setup (Aramis from GOM GmbH) to ensure homogeneous deformation without buckling during compression. The specimens were either loaded to failure or unloaded after a pre-strain of $\varepsilon_p =$ 1, 2, or 5 pct and subjected to compressive load by $\varepsilon_c = 1.5$ pct (Figure 3(a)). Since only plastic deformation is relevant for the extent of Bauschinger effect, the influence of 475 °C embrittlement on the yield strength and thus on the expansion of the elastic range was considered. For this purpose, the plastic fraction of pre-strain $\varepsilon_{p,pl}$ (Figure 3) was determined from the experimental data and used for all further analyses.

Stress–strain curves were evaluated regarding mechanical properties and, in particular, the Bauschinger effect. The onset of plastic flow during tension (σ_t) and compression (σ_c) was estimated based on the determination of yield strength in tensile tests by the intersection of the stress–strain curve with the elastic straight line shifted by 0.1 pct strain according to standard ISO 6892-1.[47] Elastic straight lines during loading and unloading were calculated using Chordal method according to technical rule ISO/TTA M2 in combination with least-square method.[48] To quantify the Bauschinger effect, the drop in yield point after load reversal was considered. In order to account for strain hardening during tensile loading and the resulting increase in flow stress during tension, Bauschinger stress σ_B was calculated according to Reference 38 as the difference between maximum stress value during tension σ_{max} and compressive yield point σ_c (Eq. [1]).

$$\sigma_B = \sigma_{max} - |\sigma_c| \quad [1]$$

In addition, plastic re-deformation $\Delta\varepsilon_p$ was calculated. Plastic re-deformation is a measure of the occurring back stresses during unloading and determined from the difference between the unloading curve and the linear-elastic straight line in zero force transition.[44,49]

Selected samples of the as-rolled condition and the 15 hours of embrittled state were further examined by scanning electron microscopy (SEM). The specimens were analyzed (i) prior deformation (position A in Figure 3), (ii) after a pure tensile load of $\varepsilon_p = 2$ pct (position B), and (iii) after tension–compression load (position C). For slip trace analysis, the curved sample surface was wet ground by SiC paper up to a grit size of P4000 and polished with diamond pastes of 6, 3, and 1 μm. Final polishing was done using a colloidal Si suspension with a grain size of 0.04 μm. For EBSD measurements, secondary samples were taken from the parallel length with the analyzed surface perpendicular to loading direction. Samples were also ground and polished up to diamond paste of 1 μm. Final polishing was performed electrolytically using Struers electrolyte A2 at a temperature of 5 °C and a voltage of 17 V for 15 seconds. Investigations were carried out on the SEM Sigma of Zeiss company. For the analysis of slip traces, the SE detector (working distance: 10 mm, voltage: 10 kV) as well as the InLens detector (working distance: 4.5 mm, voltage: 5 kV) were used. EBSD measurements were performed at a working distance of 16 mm and a voltage of 20 kV. At ×5000 magnification, an area of 150 × 100 μm was imaged with a step size of approximately 0.1 μm. The proportion of unidentified measuring spots was below 1.5 pct for all samples.

Instrumented micro-indentation tests were performed to analyze the individual phase properties of austenite and ferrite. A coarse-grained microstructure was set to

Table I. Chemical Composition of 1.4462 Duplex Stainless Steel (Wt Pct, According to Material Testing Certificate Provided by Deutsche Edelstahlwerke Specialty Steel GmbH & Co. KG)

C	Si	Mn	P	S	Cr	Mo	Ni	N
0.013	0.51	1.85	0.023	0.002	22.26	3.120	5.66	0.164

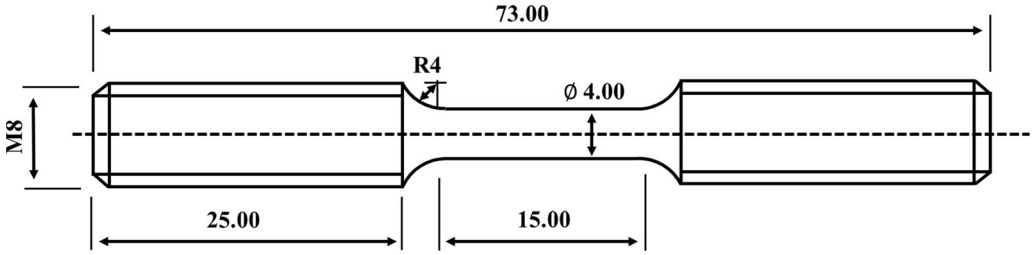

Fig. 2—Specimen geometry for tension–compression test with dimensional units in mm.

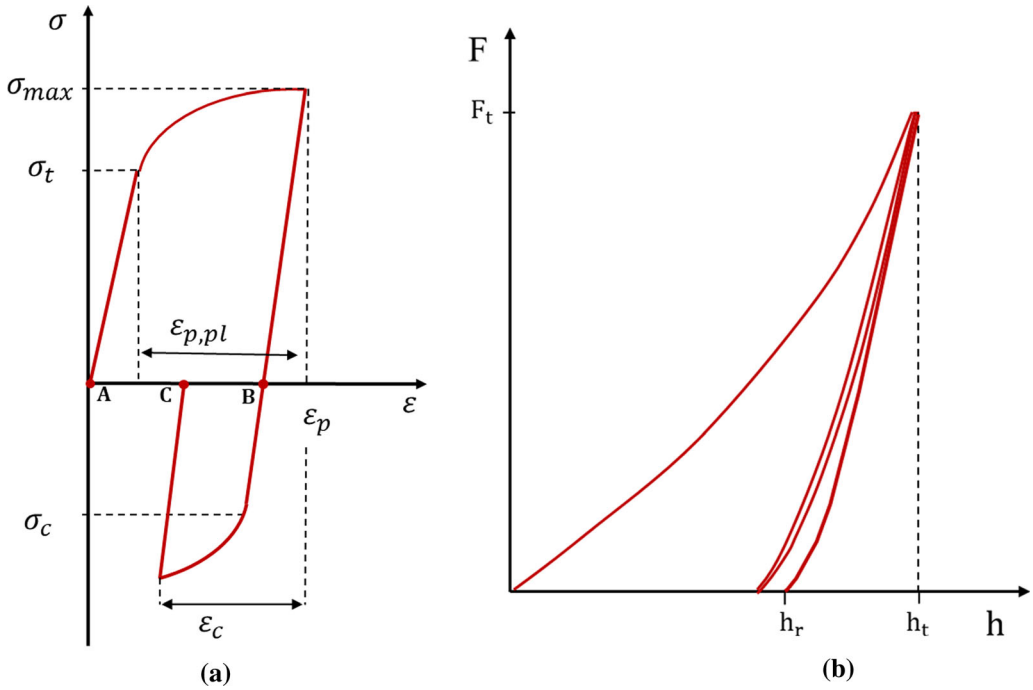

Fig. 3—(*a*) Sketch of tension–compression tests: elongation of the specimens up to maximum pre-strain $\varepsilon_p =$ 1, 2, or 5 pct followed by compression with $\varepsilon_c = 1.5$ pct. (*b*) Sketch of the force–indentation depth curve from two-cycle micro-indentation tests for quantification of the Bauschinger effect in individual austenitic and ferritic grains (maximum force F_t, maximum/permanent indentation depth h_t/h_r).

enable indentations in individual grains. Therefore, the material was annealed at 1250 °C for 5 hours, slowly cooled to 1050 °C, and quenched in water to avoid the precipitation of chromium nitrides and the sigma phase (Figure 1). The resulting microstructure contains grains with a diameter of ~ 100 μm, which are sufficiently large for micro-indentations in individual grains. Part of the samples was additionally subjected to a 475 °C embrittlement annealing analogous to the samples for tension–compression tests. The specimens were embedded, ground, and polished to a grit size of 1 μm with diamond paste. Since electrolytic polishing will remove the austenitic and ferritic phases to different degrees, but the micro-indentation test requires a planar surface, the final polishing was performed by vibration polishing in ultra-fine polishing suspension (Al_2O_3) of grain size 0.06 μm for 2 hours. Micro-indentation tests were performed using a Fischerscope HM2000 under continuous measurement of force and indentation depth. Force was applied by a Rockwell ruby ball indenter with a ball diameter of 0.4 mm, according to Reference 50. At least five measurements were performed for each material condition and test parameter, and the arithmetic mean was calculated. Microhardness was determined using monocyclic measurements with a maximum load of 500 mN and a dwell time of 5 seconds. The universal hardness HU for spherical indenters was determined analogously to the standardized Martens hardness for pyramidal indenters from the quotient of maximum load F_t and permanent indentation depth h_r.[51] The Bauschinger effect was analyzed using two-cycle micro-indentation tests, each consisting of two loadings and unloadings on the same spot (Figure 3(b)). Force was applied as a sinusoidal function with a frequency of 1/12 Hz and a maximum load of 500 mN. Relative recovery of deformation r was calculated from the unloading curves as the difference between maximum indentation depth h_t and permanent indentation depth h_r according to Eq. [2] and Figure 3(b).[52] To account for the different strength of both phases, recovery was normalized by maximum indentation depth.

$$r = \frac{h_t - h_r}{h_t} \qquad [2]$$

III. RESULTS

The microstructure of the DSS 1.4462 is shown in Figure 4 using the phase map from the EBSD data. The as-rolled condition (Figure 4(a)) is characterized by an average grain diameter of 7.9 μm. Due to grain coarsening annealing at 1250 °C for 5 hours, the average grain diameter increases to 45.7 μm (Figure 4(b)). Several grains with diameters up to approx. 100 μm can be found, which were selected for the subsequent micro-indentation tests of the individual grains.

Material properties based on tensile tests and hardness measurements are summarized in Figure 5(a) and Table II. As expected, 475 °C embrittlement leads to higher strength with increasing annealing time. Hardness, yield strength, and ultimate tensile strength increase significantly at the expense of toughness.

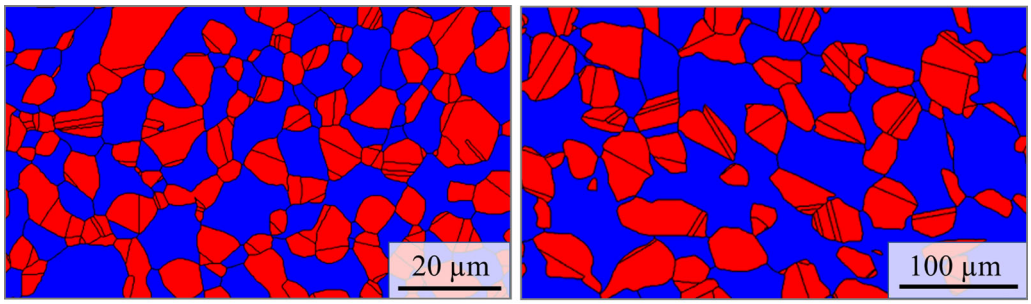

Fig. 4—Phase map of DSS 1.4462 derived from EBSD data (austenite colored in red, ferrite in blue); (*a*) as-rolled condition (ferrite 51 pct, austenite 49 pct), (*b*) grain coarsening for micro-indentation tests in single grains (annealing at 1250 °C for 5 h; ferrite 56 pct, austenite 44 pct) (Color figure online).

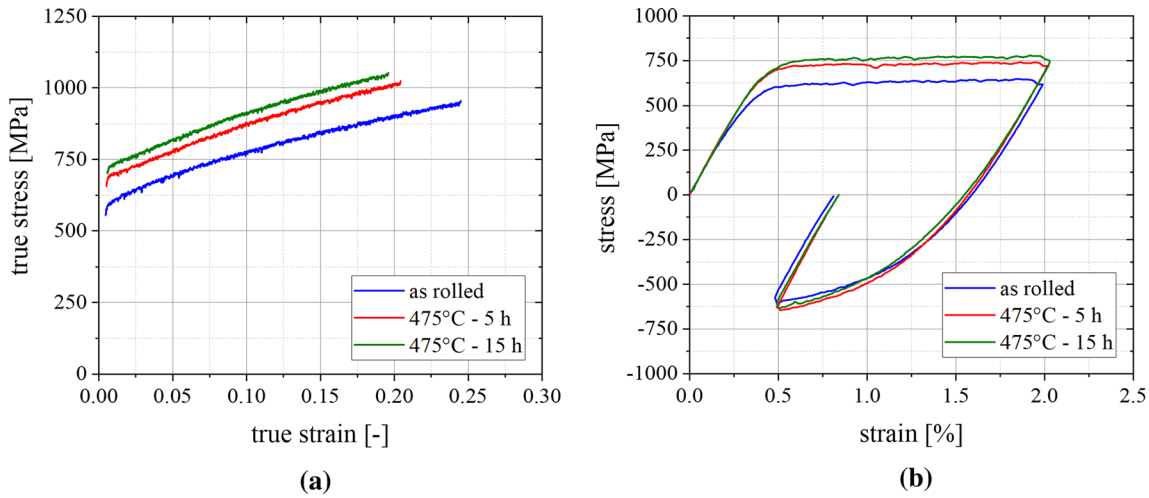

Fig. 5—Stress–strain curves from (*a*) tensile tests and (*b*) tension–compression test of DSS 1.4462 in the as-rolled and embrittled state.

Table II. Averaged Hardness Values (HV10) and Standard Deviations as Well as Parameters from Tensile Test of DSS 1.4462 in the As-Rolled and Embrittled State

Material Condition	Hardness, HV10	Tensile Strength (MPa)	Uniform Elongation (Pct)
As-Rolled	275.0 ± 1.8	757 ± 9	27 ± 2
475 °C—5 h	295.4 ± 2.5	838 ± 4	23 ± 1
475 °C—15 h	326.2 ± 2.6	868 ± 3	21 ± 1

Tension–compression tests of DSS 1.4462 have shown that even the as-rolled initial state exhibits a strongly pronounced Bauschinger effect, characterized by a decrease in yield strength of more than 58 pct (transient softening) and a homogeneous elastic–plastic transition zone during load reversal (Figure 5(b)). The increase in strength due to 475 °C embrittlement is overcompensated by an increasing Bauschinger effect with longer aging time, so that the 15-hour-aged specimen shows a lower flow stress after load reversal despite a higher strength level during initial loading. Bauschinger stress is strongly dependent on pre-strain and microstructure, as can be observed in Figure 6(a). An increase of pre-strain from 1 to 5 pct leads to a significantly earlier onset of flow during load reversal and double plastic re-deformation (Figure 6(b)). Embrittlement due to 475 °C heat treatment significantly increases the Bauschinger effect, showing a positive correlation with heat treatment time. In addition, the influence of embrittlement increases with higher pre-strain. The formation of α' precipitates leads to a significant increase in Bauschinger stress and plastic re-deformation even at small pre-strains. At higher pre-strains of 5 pct, however, the increase is considerably more pronounced (Figure 6). Thus, both influencing factors seem to reinforce each other.

Figure 7 shows the results of EBSD analysis after 2 pct tensile loading for the as-rolled and the embrittled condition (475 °C, 15 hours). The image quality (IQ) describes the distortion of diffraction pattern and can be

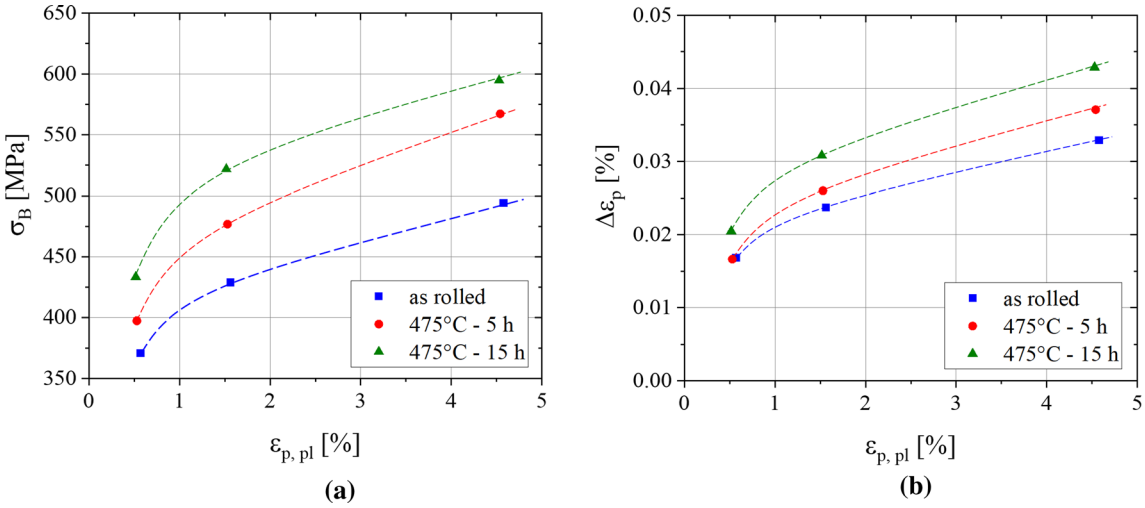

Fig. 6—(*a*) Bauschinger stress and (*b*) plastic re-deformation from tension–compression tests of DSS 1.4462 in the as-rolled and embrittled state.

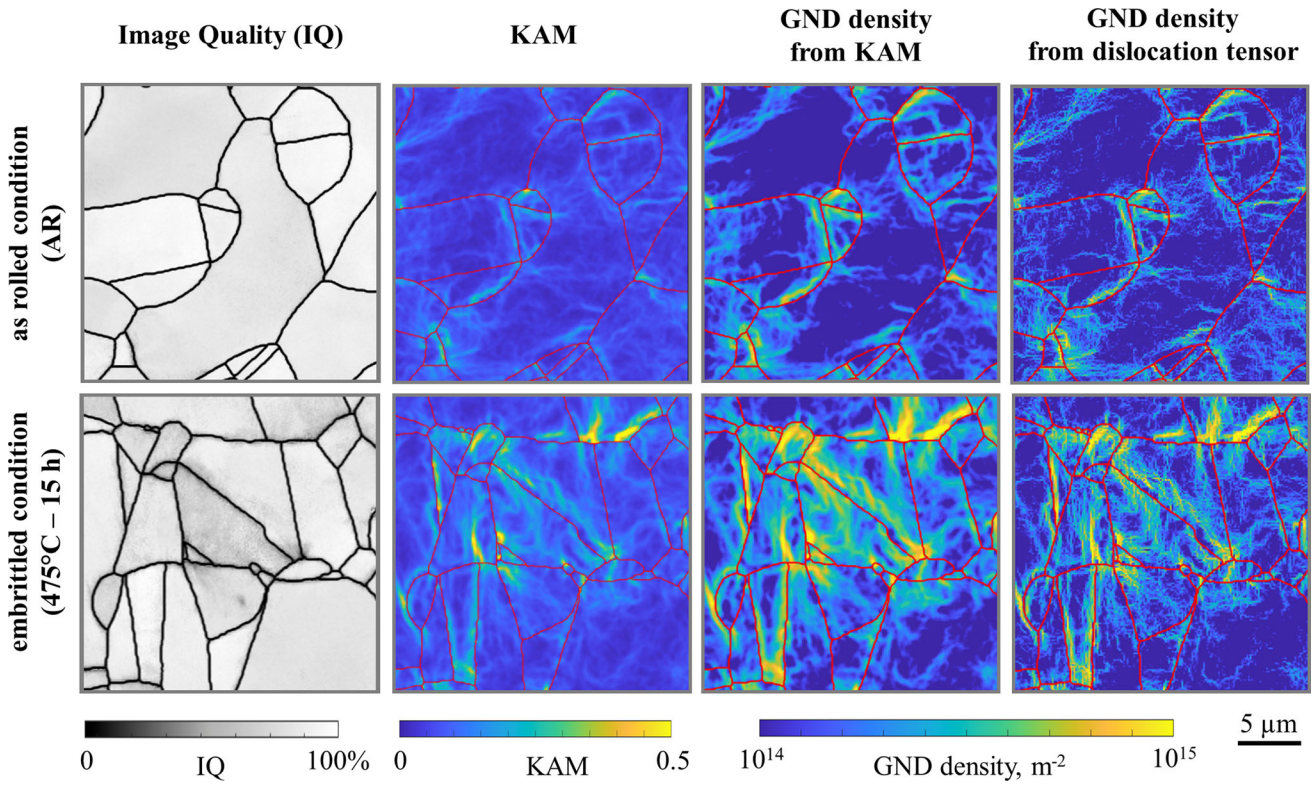

Fig. 7—EBSD analysis of DSS 1.4462 after 2 pct tensile loading. The as-rolled condition shows lower image quality (IQ) and Kernel Average Misorientation (KAM) than the embrittled condition (annealing at 475 °C for 15 h). GND density maps calculated from KAM and from dislocation tensor show similar results and indicate a higher dislocation density in the embrittled condition (grain boundaries colored red) (Color figure online).

used to estimate the overall defect density. It is thus a qualitative measure of dislocation density, representing both statistically stored dislocations (SSD) and geometrically necessary dislocations (GND). By contrast, the kernel average misorientation (KAM) is a measure for local lattice curvature and therefore represents only GNDs.[53,54] KAM value was derived from the orientation difference of a measuring point relative to surrounding measuring points, including also 2nd neighboring points. Both IQ and KAM values indicate a higher lattice distortion in the embrittled state, suggesting a higher density of SSD and GND, respectively.

Based on EBSD data, GND density was determined using two different approaches. First, GND density was calculated based on KAM value. According to the approaches of Kubin and Mortensen[55] and Gao,[56] the GND density is calculated from misorientation angle ϑ,

length of Burgers vector b, and unit length u according Eq. [3]. To estimate the misorientation angle, KAM value can be used.[54]

$$\rho_{GND} = \frac{2\vartheta}{ub} \quad [3]$$

In the second approach, GND density was calculated from the dislocation density tensor with a reduced number of components, which was derived from EBSD orientation data based on an optimization procedure implemented in MTex (Matlab R2020a). For detailed information on the procedure and the assumptions made, refer to References 54, 57, 58. The GND density calculated from dislocation tensor is slightly lower and more finely resolved than the calculations based on KAM value, since an averaging occurs when KAM value is determined by including 2nd-order neighbors. However, both methods clearly show that the embrittled ferrite grains of DSS with the resulting α' precipitates lead to a significantly higher GND density after deformation (Figure 7).

The GND density map of the embrittled condition from Figure 7 is magnified and shown in Figure 8(a) with phase identification of selected grains. The inhomogeneous distribution of GND is very evident, with austenitic grains generally exhibiting higher GND density. Especially at phase boundaries, a significant increase in dislocation density occurs in austenitic grains, whereas the adjacent ferritic grains show only a slight increase.

The inhomogeneous deformation behavior of austenite and ferrite can also be observed by the slip traces, which are created by the sets of dislocations leaving the crystal lattice and each forming a step at the height of the Burgers vector on the specimen surface (Figure 9). The overview image (Figure 9(a)) clearly shows that the austenitic grains have significantly more pronounced slip traces than the ferritic grains. This is also illustrated by the higher magnification (Figure 9(b)), showing an austenitic grain with a high density of parallel slip traces, which run through the entire grain and are only deflected at the horizontal twin boundaries. In contrast, the surrounding ferrite grains show only very weakly pronounced slip traces close to phase boundaries, which, however, fade significantly towards grain interior.

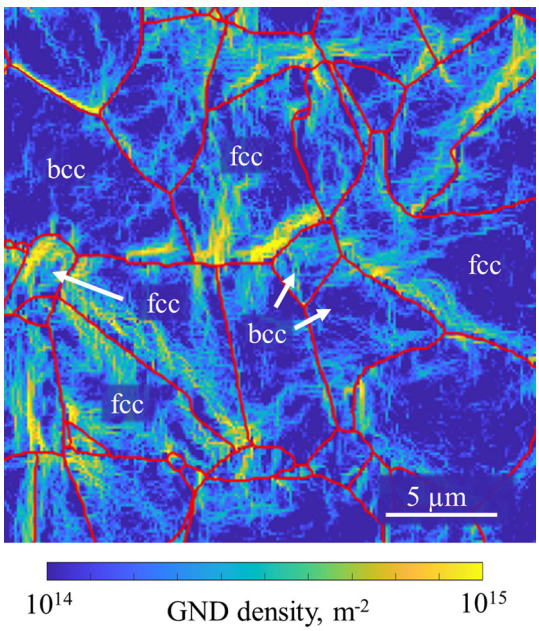

Fig. 8—GND density distribution for austenite (fcc) and ferrite (bcc) indicates inhomogeneous deformation behavior, especially at grain and phase boundaries (colored red) (Color figure online).

In order to statistically substantiate the previous analysis of slip traces and GND density maps (Figures 7 and 8), the average GND density was calculated based on KAM data from a specimen area of 150 × 100 μm^2. Figure 10(a) shows the average GND density before deformation (A), after tension (B), and after tension–compression loading (C) for different material conditions. As expected, GND density increases significantly due to plastic deformation. After tension, GND density in the embrittled condition is higher than in the initial condition. Compressive loading increases the average GND density by more than 20 pct in the as-rolled condition, whereas it remains at the same level in the embrittled condition. Figure 10(b) compares the average GND density of austenite and ferrite after a tensile loading of $\varepsilon_p = 2$ pct strain. The austenite phase exhibits a higher GND density and thus a stronger plastic deformation than the ferrite. Heat treatment and the associated strengthening due to α' precipitation increase GND density in both phases. The difference in average GND density between ferrite and austenite nearly doubles.

Figure 11(a) shows the results of instrumented micro-indentation test in single austenitic and ferritic grains. The austenite shows a similar force–indentation depth curve for all microstructures with an universal hardness of about 780 N/mm^2. By contrast, the hardness of ferrite is affected by the 475 °C embrittlement and increases from 937 in the initial state to 1024 N/mm^2 after 5 h and 1033 N/mm^2 after 15 hours, respectively. A similar pattern is shown by the relative recovery of the two-cycle indentation in Figure 11(b). Relative recovery of austenite increases only slightly by heat treatment from 0.48 to 0.53. Ferrite shows a significantly higher overall relative recovery as well as a pronounced increase from 0.73 in the initial state to 0.92 after 475 °C embrittlement for 15 hours.

IV. DISCUSSION

The Bauschinger effect in DSS 1.4462 was investigated by tension–compression tests and instrumented micro-indentation tests with particular attention on local deformation behavior investigated by EBSD analysis and dislocation density calculations. First, the Bauschinger effect and its underlying mechanisms are discussed in general terms referring to the as-rolled condition (Section IV–A). This serves as a basis for further discussion, since the as-rolled condition is used

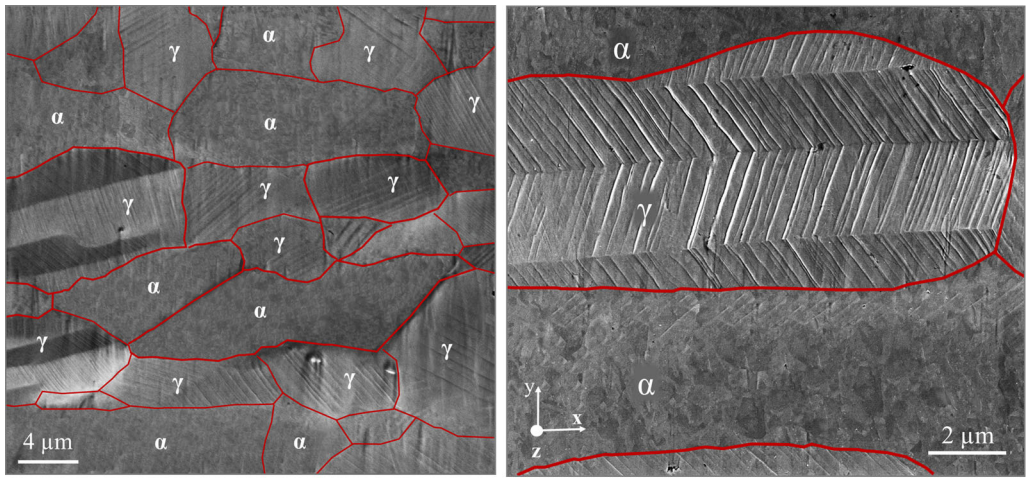

Fig. 9—SEM micrographs of DSS 1.4462 after deformation: Austenite (γ) shows strongly pronounced parallel slip traces, whereas the surrounding ferrite (α) show only slight slip traces close to phase boundaries; (load axis in z-direction, specimen surface was polished prior to deformation);.

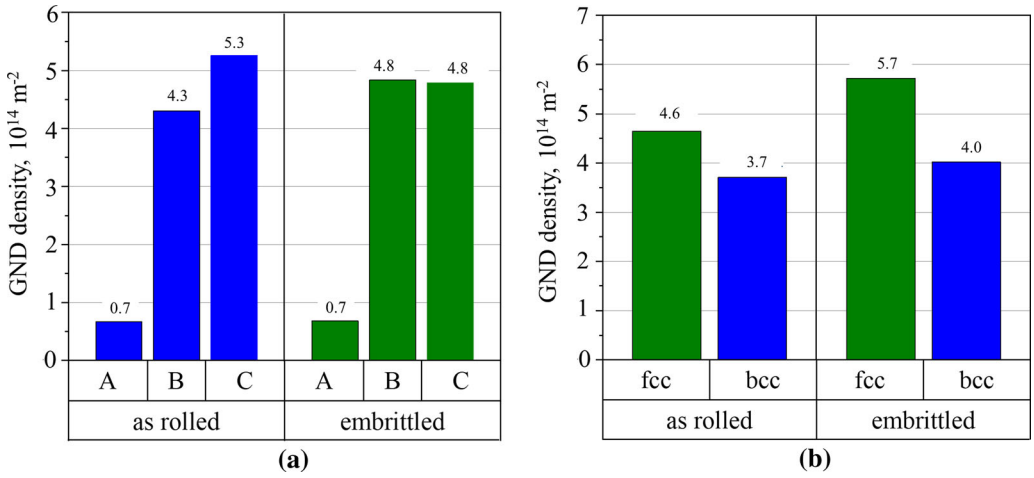

Fig. 10—Average GND density of DSS 1.4462 in the as-rolled and embrittled state (*a*) at different stages during tension–compression test: before deformation (A), after $\varepsilon_p = 2$ pct tension loading (B), and after $\varepsilon_c = 1.5$ pct compression loading (C, see Fig. 3); (*b*) for austenitic and ferritic phase fraction after $\varepsilon_p = 2$ pct tensile strain.

as a reference state for microstructural modifications. Major focus of the discussion will be on the effects of phase-selective α' precipitates formed in the ferritic phase during 475 °C embrittlement (Section IV–B). The influence on the Bauschinger effect is quantified and analyzed considering local plasticity behavior, especially at phase boundaries. Finally, it is investigated whether pre-deformation influences the impact of α' precipitation on Bauschinger effect and whether there are cross-relationships between both influencing factors (Section IV–C).

A. *Bauschinger Effect and Its Causes in DSS*

Tension–compression tests have demonstrated that DSS 1.4462 exhibits a strongly pronounced Bauschinger effect, with a drop in yield point of more than 58 pct in the as-rolled condition. In general, the pronounced Bauschinger effect in multi-phase alloys is mainly attributed to heterogeneous deformation behavior and the resulting back stresses.[38,39,59] The DSS examined in this study shows a significant difference in local mechanical properties with 20 pct higher hardness of the ferritic phase. This leads to a partitioning of stress and strain during tensile loading. The ferrite experiences high stresses, which can be predominantly elastic at low tensile pre-strain, whereas a higher strain level is observed in the austenite. The inhomogeneous distribution of stress and strain generates internal residual stresses, which lead to the Bauschinger effect during load reversal.[30,31,38] The partitioning of stress and strain is particularly visible at the phase boundaries, where it leads to pronounced deformation incompatibilities. Slip trace analysis, KAM maps, and GND density maps of the deformed specimens confirm the inhomogeneous deformation behavior. The austenitic phases shows a 32

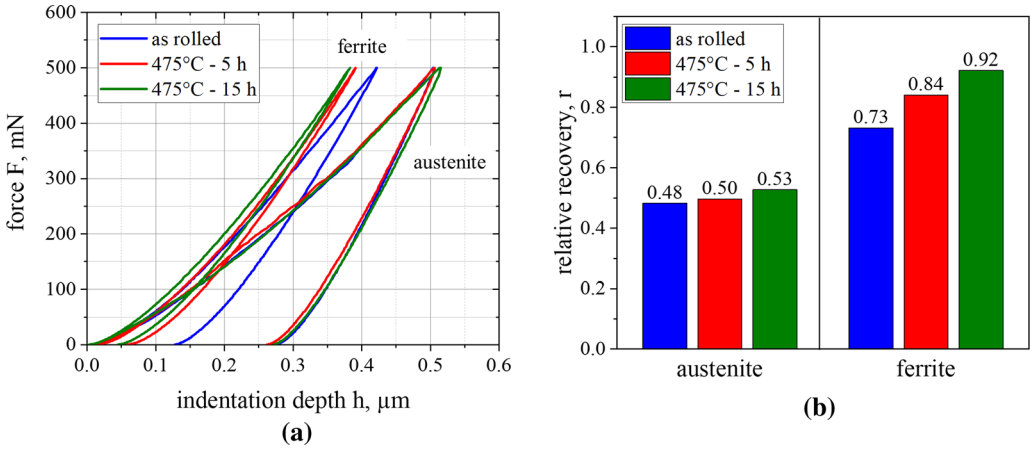

Fig. 11—Micro-indentation tests in single austenite and ferrite grains. (*a*) force–indentation depth curves of one-cycle indentation tests (hardness measurement) and (*b*) relative recovery of two-cycle indentation tests (Bauschinger effect) for different microstructures of DSS 1.4462 in the as-rolled and embrittled state.

pct higher GND density and thus more pronounced deformation than ferrite, which is assumed to result from stress and strain partitioning between both phases. Furthermore, local deformation gradients between the grain interior and the grain boundary can be identified. In particular phase boundaries show more pronounced slip traces and significantly increased GND density (Figure 8), indicating deformation incompatibility and back stresses. These back stresses are assumed to promote dislocation movement during re-deformation and cause the pronounced Bauschinger effect observed in tension–compression tests (Figures 5 and 6).

B. *Effect α′ Precipitates on Bauschinger Effect (475 °C Embrittlement)*

Tension–compression tests have shown that the Bauschinger effect is significantly affected by α′ precipitates due to 475 °C embrittlement, which is reflected in an increase in Bauschinger stress of up to 20 pct. At first sight, this contradicts the general assumption that small coherent precipitates with a size of a few nanometers only have a minor influence on the Bauschinger effect.[17,18,20] The pronounced Bauschinger effect can therefore be explained in part but not exclusively by the direct effect of α′ precipitates. Rather, it is hypothesized that the inhomogeneous, phase-selective precipitation of α′ precipitates in ferrite plays an essential role. In the following, both effects are discussed using micro-indentation tests and EBSD measurements of the deformed samples, both in the as-rolled and the embrittled condition. First, the direct effect of α′ precipitates by dislocation interaction is discussed. Second, an enhancement of the elastic–plastic phase difference between austenite and ferrite caused by phase-selective precipitation is analyzed.

The direct influence of α′ precipitates on the Bauschinger effect was quantified using cyclic micro-indentation tests in single austenitic and ferritic grains. As expected, the Bauschinger effect of the austenitic phase does not change significantly, since austenite is not affected by 475 °C embrittlement. In contrast, the ferritic grains show a significant increase in relative recovery and thus Bauschinger effect. The causal influence of α′ precipitates on deformation behavior is evident from the development of average GND density during tension–compression loading. The as-rolled condition shows a significant increase in GND density due to load reversal. High dislocation density is accompanied by a high yield point at load reversal and thus a weak Bauschinger effect. In comparison, the embrittled state shows a higher dislocation density after tensile loading, which can be explained by the strength-increasing effect of α′ precipitates resulting from obstructing dislocation movement. Due to the small spacing of α′ precipitates, mean free path length of dislocation movement decreases, requiring higher activity of dislocation sources to maintain plastic deformation. However, dislocation density does not further increase during load reversal (Figure 10). This is consistent with the theory that accumulated dislocations in front of precipitates are mobile in backward direction and support plastic deformation during reverse loading.[15] Furthermore, α′ precipitates are assumed to create short-range internal stress fields, which promote dislocation movement and thus enhance the Bauschinger effect. The influence of these phenomena can be estimated by the observed increase in Bauschinger effect based on cyclic micro-indentations in individual ferritic grains (Figure 11).

It is assumed that, in addition to the described short-range effect of the dislocation interaction, α′ precipitates also have a long-range and thus significantly stronger effect due to the enhancement of local deformation incompatibility between austenite and ferrite. Micro-indentations in individual austenitic and ferritic grains (Figure 11) verify the increase in deformation incompatibility due to spinodal decomposition of the ferrite. The microhardness of ferrite increases by more than 10 pct due to 475 °C embrittlement, whereas austenite is not affected. The increasing difference of elastic plastic phase properties directly affects load

partitioning between the two phases. The phase difference in average GND density after deformation nearly doubles due to 475 °C embrittlement (Figure 10). Also EBSD analyses, comprising IQ, KAM value, and GND density maps, clearly show the influence on local plasticity behavior. The formation of α' precipitates significantly increases local misorientation and GND density, especially at phase boundaries. These local gradients are associated with internal back stresses, which may explain the pronounced Bauschinger effect.

C. *Effect of Pre-deformation on Bauschinger Effect*

Tension–compression tests show an increase of the Bauschinger effect with increasing pre-strain in the analyzed interval between 1 and 5 pct pre-strain, which is in good agreement with existing literature knowledge.[10] However, it is worth mentioning that a slight interdependence between the influence of pre-strain and α' precipitates can be identified. The influence of α' precipitates on Bauschinger effect increases with higher pre-strain, for which different explanations can be considered. On the one hand, increasing dislocation density can be again mentioned as possible reason, since it increases the pile-up in front of precipitates and thus strengthens their effect on deformation behavior. On the other hand, strain dependency of load partitioning within the two-phase microstructure could be a reason. Investigations by Reference 29 on tensile specimens show that deformation behavior up to a plastic strain of $\varepsilon_{pre,pl} = 1.15$ pct is largely determined by the austenitic phase, whereas the influence of ferrite becomes significant only at higher strains levels. It is therefore reasonable to assume that also in the case of cyclic loading, the influence of ferrite is less pronounced at lower strains. This would explain why the effect of embrittlement on Bauschinger effect is more pronounced at higher strains, as shown by the tension–compression tests.

V. CONCLUSION

Tension–compression tests on the duplex stainless steel 1.4462 show a strongly pronounced Bauschinger effect, characterized by an early onset of plastic flow during load reversal. Micro-indentation tests in single austenitic and ferritic grains imply that a major reason is the difference in elastic–plastic properties of both phases. The analysis of local GND density based on EBSD measurements confirms a strongly inhomogeneous deformation behavior, which results in pronounced back stresses at phase boundaries. In addition, it was found that nanoscale α' precipitates due to 475 °C embrittlement lead to a significant increase in Bauschinger effect. On the one hand, micro-indentation experiments demonstrated that 475 °C embrittlement amplifies the phase difference, since it leads to the formation of precipitates only in ferrite. The resulting stronger deformation incompatibility enhances back stresses and facilitates dislocation motion during load reversal. On the other hand, α' precipitates themselves lead to a stronger Bauschinger effect in the ferritic phase. Dislocation pile-up during initial loading reduces the necessity of dislocation formation upon load reversal, as indicated by the change in average GND density prior and post compressive loading. The availability of mobile dislocations as well as reduced dislocation formation macroscopically result in a strongly pronounced Bauschinger effect, as can be seen by tension–compression tests. The data obtained provide important insights into the plasticity behavior of duplex steels and will be used for the simulative analysis of Bauschinger effect in multi-phase alloys by means of a single crystal plasticity model with latent kinematic hardening (ongoing work, publication in preparation).

ACKNOWLEDGMENTS

The authors would like to thank N. Babaei and Dr. D. Wipp from RWTH Aachen University (Germany) for valuable discussions. Specimen material provided by Deutsche Edelstahlwerke Specialty Steel GmbH & Co. KG and financial support by the Deutsche Forschungsgemeinschaft DFG (project number KR 1999/25) are gratefully acknowledged.

AUTHOR CONTRIBUTIONS

MK: Conceptualization, Methodology, Investigation, Writing—Original Draft, and Visualization. JW: Conceptualization, Methodology, and Investigation. SW: Writing—Review & Editing. UK: Conceptualization, Writing—Review & Editing, Supervision, and Funding acquisition.

FUNDING

Open Access funding enabled and organized by Projekt DEAL.

DATA AVAILABILITY

The raw/processed data required to reproduce the findings in the study cannot be shared at this time, as the data also form part of several ongoing studies. However, the data may be made available from the corresponding author upon request.

COMPETING INTEREST

The authors declare that they have no known competing financial interests or personal relationships that could have appeared to influence the work reported in this paper.

REFERENCES

1. J. Bauschinger: *Über die Veränderung der Elastizitätsgrenze und der Festigkeit des Eisens und Stahls durch Strecken und Quetschen, durch Erwärmen und Abkühlen und durch oftmals wiederholte Beanspruchung*. Communication, Munich, Germany, 1886.
2. S.M. Kamal: *Mechanics Based Design of Structures and Machines*, 2020, pp. 1–20.
3. D.W. Kim, S.S. Sohn, W.-K. Kim, K.-S. Kim, and S. Lee: *Sci. Rep.*, 2018, vol. 8, p. 15598.
4. S. Suresh: *Fatigue of Materials*, 2nd ed. Cambridge Univ. Press, Cambridge, 2004.
5. L.E. Levine, M.R. Stoudt, A. Creuziger, T.Q. Phan, R. Xu, and M.E. Kassner: *J. Mater. Sci.*, 2019, vol. 54, pp. 6579–85.
6. M.W. Kapp, C. Kirchlechner, R. Pippan, and G. Dehm: *J. Mater. Res.*, 2015, vol. 30, pp. 791–97.
7. M.G. Stout and A.D. Rollett: *Metall. Mater. Trans. A*, 1990, vol. 21A, pp. 3201–13.
8. T. Hasegawa, T. Yakou, M. Shimizu, and S. Karashima: *Trans. JIM*, 1976, vol. 17, pp. 414–18.
9. K. Han, C.J. van Tyne, and B.S. Levy: *Metall. Mater. Trans. A*, 2005, vol. 36A, pp. 2379–84.
10. A. Abel and H. Muir: *Philos. Mag.*, 1972, vol. 26, pp. 489–504.
11. S.Y. Han, S.S. Sohn, S.Y. Shin, J. Bae, H.S. Kim, and S. Lee: *Mater. Sci. Eng., A*, 2012, vol. 551, pp. 192–99.
12. Y.S. Danilov: *Met. Sci. Heat Treat.*, 1964, vol. 6, pp. 563–65.
13. M. Kreins, S. Schilli, T. Seifert, A. Iyer, M.H. Colliander, S. Wesselmecking, and U. Krupp: *Mater. Sci. Eng. A*, 2021, vol. 827, p. 142027.
14. S. Schilli, T. Seifert, M. Kreins, and U. Krupp: *Mater. Sci. Eng. A*, 2022, vol. 830, p. 142030.
15. A.G. Kostryzhev, M. Strangwood, and C.L. Davis: *Ironmak. Steelmak.*, 2009, vol. 36, pp. 186–92.
16. J.D. Atkinson, L.M. Brown, and W.M. Stobbs: *Philos. Mag.*, 1974, vol. 30, pp. 1247–80.
17. A.G. Kostryzhev, M. Strangwood, and C.L. Davis: *Metall. Mater. Trans. A*, 2010, vol. 41A, pp. 1399–1408.
18. S. Queyreau and B. Devincre: *Philos. Mag. Lett.*, 2009, vol. 89, pp. 419–30.
19. R.E. Stoltz and R.M. Pelloux: *Metall. Mater. Trans. A*, 1976, vol. 7A, pp. 1295–1306.
20. S. Ghorbanpour, M. Zecevic, A. Kumar, M. Jahedi, J. Bicknell, L. Jorgensen, I.J. Beyerlein, and M. Knezevic: *Int. J. Plast*, 2017, vol. 99, pp. 162–85.
21. J.K. Sahu, U. Krupp, R.N. Ghosh, and H.-J. Christ: *Mater. Sci. Eng. A*, 2009, vol. 508, pp. 1–4.
22. R.N. Gunn: *Duplex Stainless Steels: Microstructure, Properties and Applications*, Abington Publishing, Cambridge, 1997.
23. I. Alvarez-Armas and S. Degallaix-Moreuil: *Duplex Stainless Steels*, Wiley, Hoboken, 2009.
24. F.A. Alhegagi: *Int. J. Sci. Eng. Res.*, 2015, vol. 6, pp. 145–54.
25. C. Örnek, M.G. Burke, T. Hashimoto, and D.L. Engelberg: *Metall. Mater. Trans. A*, 2017, vol. 48A, pp. 1653–65.
26. International Molybdenum Association: *Practical Guidelines for the Fabrication of Duplex Stainless Steels*, 2nd ed. IMOA, London, 2009.
27. K. Weng, H. Chen, and J. Yang: *Mater. Sci. Eng. A*, 2004, vol. 379, pp. 119–32.
28. J. Mizera, Z. Pakiela, P. Maj, and J. Zdunek: in *Proceedings of the 2017 IEEE 7th International Conference on Nanomaterials: Applications & Properties (NAP-2017)*, ed. by A. D. Pogrebnjak, Zatoka, Ukraine, September 10–15, 2017, IEEE, Piscataway, 2017.
29. I. Serre, D. Salazar, and J.-B. Vogt: *Mater. Sci. Eng. A*, 2008, vol. 492, pp. 428–33.
30. S. Harjo, Y. Tomota, P. Lukáš, D. Neov, M. Vrána, P. Mikula, and M. Ono: *Acta Mater.*, 2001, vol. 49, pp. 2471–79.
31. S. Harjo, P. Lukáš, Y. Tomota, D. Neov, M. Vrána, P. Mikula, and M. Ono: *MSF*, 2000, vol. 347–349, pp. 328–33.
32. S. Wroński, J. Tarasiuk, B. Bacroix, A. Baczmański, and C. Braham: *Mater Charact*, 2012, vol. 73, pp. 52–60.
33. U. Krupp, O. Düber, H.-J. Christ, B. Künkler, P. Köster, and C.-P. Fritzen: *Mater. Sci. Eng. A*, 2007, vol. 462, pp. 174–77.
34. S.K. Paul and A. Kumar: *Comput. Mater. Sci.*, 2012, vol. 63, pp. 66–74.
35. U. Krupp and I. Alvarez-Armas: *Int. J. Fatigue*, 2014, vol. 65, pp. 78–85.
36. U. Krupp, A. Giertler, M. Söker, H. Fu, B. Dönges, H.-J. Christ, K. Istomin, A. Hüsecken, U. Pietsch, C.-P. Fritzen, and W. Ludwig: *Procedia Eng.*, 2014, vol. 74, pp. 143–46.
37. U. Krupp, A. Giertler, M.C. Marinelli, and H. Knobbe: *Efficiency of Grain and Phase Boundaries as Microstructural Barriers During HCF and VHCF Loading of Austenitic-Ferritic Duples Steel*, Berlin, Germany, 2011.
38. S. Harjo, Y. Tomota, D. Neov, P. Lukas, M. Vrana, and P. Mikula: *ISIJ Int.*, 2002, vol. 42, pp. 551–57.
39. B. Verhaeghe, Y. Brechet, F. Louchet, J.P. Massoud, and D. Touzeau: *Phys. Stat. Sol. A*, 1996, vol. 153, pp. 47–56.
40. U. Krupp, M. Söker, A. Giertler, B. Dönges, H.-J. Christ, K. Wackermann, T. Boll, M. Thuvander, and M.C. Marinelli: *Int. J. Fatigue*, 2016, vol. 93, pp. 363–71.
41. DIN Deutsches Institut für Normung e.V., *Stainless Steels: Part 3: Technical Delivery Conditions for Semi-finished Products, Bars, Rods, Wire, Sections and Bright Products of Corrosion Resisting Steels for General Purposes* (Beuth Verlag GmbH, Berlin, 2014), ICS 77.140.20; 77.140.50; 77.140.65, DIN EN 10088-3.
42. S. Kobayashi and T. Takasugi: *Scripta Mater.*, 2010, vol. 63, pp. 1104–07.
43. DIN—German Institute for Standardization, *Metallic Materials—Vickers Hardness Test: Part 1: Test Method* (Beuth Verlag GmbH, Berlin, 2006), vol. 77.040.10, DIN EN ISO 6507-1:2015.
44. B. Scholtes, O. Vöhringer, and E. Macherauch: *Steel Res.*, 1985, vol. 56, pp. 157–62.
45. S.F. Corbin, D.S. Wilkinson, and J.D. Embury: *Mater. Sci. Eng. A*, 1996, vol. 207, pp. 1–11.
46. Deutsches Institut für Normung, *Prüfung metallischer Werkstoffe—Zugproben* (Beuth, Berlin, 2016), vol. 77.040.10, DIN 50125.
47. Deutsches Institut für Normung, *Metallic Materials—Tensile Testing: Part 1: Method of Test at Room Temperature* (Beuth Verlag GmbH, Berlin, 2017), vol. 77.040.10, DIN EN ISO 6892-1:2016.
48. ISO, ISO/TTA 2:1997: Tensile tests for discontinuously reinforced metal matrix composites at ambient temperatures (1997), https://www.iso.org/obp/ui/#iso:std:iso:tta:2:ed-1:v1:en.
49. A. Ellermann: *Forschungsberichte aus dem Institut für Werkstofftechnik Metallischer Werkstoffe der Universität Kassel*, ed. by B. Scholtes (Kassel University Press GmbH, Kassel, 2013), pp. 1–243.
50. Deutsches Institut für Normung e.V., *Metallic Materials—Rockwell Hardness Test: Part 2: Verification and Calibration of Testing*

Machines and Indenters (Beuth Verlag GmbH, Berlin, 2015), vol. 77.040.10, DIN EN ISO 6508-2:2015.
51. Deutsches Institut für Normung e.V., *Metallic Materials—Instrumented Indentation Test for Hardness and Materials Parameters: Part 1: Test Method* (Beuth Verlag GmbH, Berlin, 2015), vol. 77.040.10, DIN EN ISO 14577-1:2015.
52. N. Huber and C. Tsakmakis: *J. Mater. Res.*, 1998, vol. 120, pp. 143–48.
53. E. Demir and D. Raabe: *Acta Mater.*, 2010, vol. 58, pp. 6055–63.
54. M. Calcagnotto, D. Ponge, E. Demir, and D. Raabe: *Mater. Sci. Eng. A*, 2010, vol. 527, pp. 2738–46.
55. L.P. Kubin and A. Mortensen: *Scripta Mater.*, 2003, vol. 48, pp. 119–25.
56. H. Gao, Y. Huang, W.D. Nix, and J. Hutchinson: *J. Mech. Phys. Solids*, 1999, vol. 47, pp. 1239–63.
57. S.A.H. Motaman, F. Roters, and C. Haase: *Acta Mater.*, 2020, vol. 185, pp. 340–69.
58. W. Pantleon: *Scripta Mater.*, 2008, vol. 58, pp. 994–97.
59. M. Weiss, A. Kupke, P.Y. Manach, L. Galdos, and P.D. Hodgson: *Mater. Sci. Eng. A*, 2015, vol. 643, pp. 127–36.